



Cite this: *Dalton Trans.*, 2015, **44**, 16946

## MOF-derived self-assembled ZnO/Co<sub>3</sub>O<sub>4</sub> nanocomposite clusters as high-performance anodes for lithium-ion batteries

Dequan Zhu,<sup>a,c</sup> Fangcai Zheng,<sup>b,c</sup> Shihao Xu,<sup>b</sup> Yuanguang Zhang<sup>b</sup> and Qianwang Chen<sup>\*c</sup>

Although different kinds of metal oxide nanoparticles are extensively investigated as anode materials for lithium-ion batteries (LIBs), their cycle life and energy/power density are still not suitable for commercial applications. Metal oxides have a large storage capacity, but they suffer from low electrical conductivity and severe volume change during the charge/discharge process. Herein, we present a facile route to prepare self-assembled ZnO/Co<sub>3</sub>O<sub>4</sub> nanocomposite clusters through calcination of preformed Prussian Blue Analogue (PBA) Zn<sub>3</sub>[Co(CN)<sub>6</sub>]<sub>2</sub> nanospheres. These self-assembled ZnO/Co<sub>3</sub>O<sub>4</sub> nanocomposite clusters exhibit superior lithium storage capabilities with good cycling properties. A reversible capacity of 957 mA h g<sup>-1</sup> was retained at a current density of 100 mA g<sup>-1</sup> up to 100 cycles. The enhanced electrochemical performance of the ZnO/Co<sub>3</sub>O<sub>4</sub> nanocomposite anode can be ascribed to the rational design of the self-assembled cluster structures and the synergetic effect of two-component functional nanoparticle systems.

Received 15th June 2015,  
Accepted 21st August 2015

DOI: 10.1039/c5dt02271a

www.rsc.org/dalton

### 1. Introduction

For the extensive applications of lithium-ion batteries (LIBs) in electric vehicles and power grids, high-performance electrode materials with high energy/power densities and good cyclic stabilities need to be developed.<sup>1,2</sup> In the last two decades, transition metal oxides based on conventional reactions have been extensively investigated as promising anode materials (*e.g.*, Co<sub>3</sub>O<sub>4</sub>,<sup>3</sup> Fe<sub>2</sub>O<sub>3</sub>,<sup>4</sup> NiO,<sup>5</sup> Mn<sub>2</sub>O<sub>3</sub>,<sup>6</sup> MnO,<sup>7</sup> and Ni<sub>x</sub>Co<sub>3-x</sub>O<sub>4</sub><sup>8</sup>) because they have higher theoretical specific capacities than that of commercial graphite (372 mA h g<sup>-1</sup>). Recently, among transition metal oxides, nanostructured ZnO and ternary Zn-based oxides (*e.g.*, ZnMn<sub>2</sub>O<sub>4</sub>, ZnFe<sub>2</sub>O<sub>4</sub> and ZnCo<sub>2</sub>O<sub>4</sub>) have attracted much attention as promising anode materials for LIBs because of their high specific capacity, low cost, and environmental friendliness.<sup>9-12</sup> However, transition metal oxides often suffer from serious capacity loss during the charge/discharge process due to the large volume variation

and slow diffusion of lithium ions and electrons in the active materials. As a consequence, considerable efforts have recently been focused on searching for alternative electrode materials with unique structures to solve the inherent poor electrical conductivity and large volume changes upon cycling, resulting in limited rate performances and rapid capacity fading.<sup>13-15</sup> Rational design and facile synthesis of Zn-based oxide electrode materials with novel structures for highly reversible and high-rate lithium storage still remain a significant challenge.

Metal-organic frameworks (MOFs) or porous coordination polymers (PCPs) have attracted particular attention in recent years as a new class of hybrid nanoporous materials created from supramolecular assembly of inorganic components (metal ions or metal clusters) with organic components (organic or organometallic complexes) because of their diverse structural topologies and tunable functionalities.<sup>16,17</sup> They have shown a wide variety of promising applications in catalysis, biomedical imaging, drug delivery, and gas separation and storage.<sup>18-20</sup> Motivated by their high surface areas, unique structures, and tunable metal ions and organic ligands, MOFs can be applied as effective self-sacrificial templates or precursors to construct novel nanoarchitectures with intriguing properties.<sup>21,22</sup> Since the MOF-5 framework (Zn<sub>4</sub>O(OOCC<sub>6</sub>H<sub>4</sub>COO)<sub>3</sub>) was employed as the template for the synthesis of porous carbon materials, several other kinds of MOFs have been used as templates or precursors to prepare porous carbon materials, metal oxides and their composites.<sup>23,24</sup> For example, our

<sup>a</sup>School of Physics and Electronic Engineering, Anqing Normal University, Anqing 246052, China

<sup>b</sup>College of Chemistry and Chemical Engineering, Anqing Normal University, Anqing 246052, China

<sup>c</sup>Hefei National Laboratory for Physical Science at Microscale, Department of Materials Science & Engineering & High Magnetic Field Laboratory, University of Science and Technology of China, Hefei 230026, China. E-mail: cqw@ustc.edu.cn; Fax: +86 551 63603005; Tel: +86 551 63603005

group firstly used Prussian blue analogues  $\text{Co}_3[\text{Co}(\text{CN})_6]_2$  as a sacrificial template and precursor for the direct synthesis of  $\text{Co}_3\text{O}_4$  nanocages,<sup>25</sup> and also synthesized high nitrogen-doped carbon materials through direct carbonization of high nitrogen-containing MOFs (ZIF-8).<sup>26</sup> Lou's group also reported large-scale synthesis of  $\text{Fe}_2\text{O}_3$  microboxes through direct calcination of preformed Prussian blue  $\text{Fe}_4[\text{Fe}(\text{CN})_6]_3$ .<sup>27</sup> More importantly, these MOF-derived metal oxides or carbon materials exhibit enhanced electrochemical performance when evaluated as anode materials for LIBs. Moreover, binary metal oxides can be obtained through direct calcination of MOF precursors containing two different metal centers, and exhibit excellent Li storage performance.<sup>17,20</sup> However, there has rarely been success in employing this strategy to prepare self-assembled  $\text{ZnO}/\text{Co}_3\text{O}_4$  nanocomposite clusters as anode materials for LIBs. Therefore, it is desirable to design and synthesize a suitable MOF as the precursor for targeted self-assembled  $\text{ZnO}/\text{Co}_3\text{O}_4$  nanocomposite clusters as anode materials for LIBs.

Herein, we demonstrate a facile strategy for the fabrication of self-assembled  $\text{ZnO}/\text{Co}_3\text{O}_4$  nanocomposite clusters using PBA  $\text{Zn}_3[\text{Co}(\text{CN})_6]_2$  nanospheres as both the precursor and the self-sacrificing template. The synthesis process only involves a room-temperature reaction to form PBA  $\text{Zn}_3[\text{Co}(\text{CN})_6]_2$  nanospheres in a solution followed by thermal annealing in air. This strategy is easy, tunable, and cost-effective, and therefore it is highly promising for mass production. Moreover, the Zn and Co atoms are uniformly arranged in the  $\text{Zn}_3[\text{Co}(\text{CN})_6]_2$  crystal framework and separated with organic linkers, which facilitate the formation of ultrafine metal oxide nanocomposites during the calcination process in air. A large number of N and C atoms from organic linkers can also be oxidized into gaseous molecules, resulting in interconnected porous structures. When evaluated as an anode material for LIBs, the porosity and synergistic effect of ZnO and  $\text{Co}_3\text{O}_4$  result in this composite exhibiting an excellent electrochemical performance.

## 2. Experimental section

### Material preparation

All chemicals are of analytical grade, and were used without any further purification. The typical synthetic experiments were performed as follows: 0.08 mmol (0.0166 g)  $\text{K}_3[\text{Co}(\text{CN})_6]_2$  and 0.3 g PVP were dissolved in 10 ml of distilled water under vigorous stirring to obtain an absolutely transparent solution. And then 10 ml solution of 0.075 mmol (0.0171 g)  $\text{ZnCl}_2 \cdot n\text{H}_2\text{O}$  was added into the above solution slowly and regularly using a syringe. The whole reaction process was maintained at room temperature with vigorous stirring. After 10 min, the reaction was aged at room temperature without any interruption for 24 h. The resulting white precipitate was collected by centrifugation, washed several times with distilled water and ethanol, and finally dried in an oven at 60 °C. Finally, porous  $\text{ZnO}/\text{Co}_3\text{O}_4$  nanocomposite clusters were successfully obtained through direct calcination of the as-synthesized  $\text{K}_3[\text{Co}(\text{CN})_6]_2$

precursor at 500 °C in air for 2 h with a temperate ramp rate of 10 °C min<sup>-1</sup>.<sup>28</sup>

### Material characterization

The powder X-ray diffraction (XRD) patterns were recorded on a Japan Rigaku D/MAX-cAX-ray diffractometer equipped with Cu K $\alpha$  radiation over the 2 $\theta$  range of 10–70°. Transmission electron microscopy (TEM) images were obtained using a Hitachi H-800 transmission electron microscope, using an accelerating voltage of 200 kV. Field emission scanning electron microscopy (FESEM) images were obtained on a JEOL JSM-6700 M scanning electron microscope. Thermogravimetric analysis (TGA) was carried out using a Shimadzu-50 thermoanalyser under air gas flow at 10 °C min<sup>-1</sup> in the temperature range 30–800 °C. Specific surface areas were computed from the results of  $\text{N}_2$  physisorption at 77 K (Micromeritics ASAP 2020) by using the BET (Brunauer–Emmett–Teller) and BJH (Barrett–Joyner–Halenda) methods.

### Electrochemical measurements

The electrochemical measurement of the as-prepared  $\text{ZnO}/\text{Co}_3\text{O}_4$  nanocomposite clusters was examined using CR2032 coin type cells vs. Li with 1 M  $\text{LiPF}_6$  in ethylene carbonate and diethyl carbonate (EC : DEC = 1 : 1, v/v) as the electrolyte. The working electrode was fabricated by compressing a mixture of active materials, conductive materials (acetylene black, ATB), and binder (polyvinylidene fluoride (PVDF)) in a weight ratio of  $\text{ZnO}/\text{Co}_3\text{O}_4$  nanocomposites/carbon/PVDF = 5 : 3 : 2 onto a copper foil current collector. The cells were assembled in an argon-filled glove box (Mikrouna, Super(1220/750/900)). The density of the active material was about 1 mg cm<sup>-2</sup> and the film thickness was about 100  $\mu\text{m}$ . The electrode capacity was measured by a galvanostatic discharge–charge method in the voltage range between 0.01 and 3.0 V on a battery test system (Neware CT-3008W).

## 3. Results and discussion

The crystallographic structure and phase purity of the as-synthesized precursor were examined by X-ray powder diffraction (XRD). Fig. 1a shows the XRD pattern of the as-synthesized precursor. All the diffraction peaks can be readily indexed as a pure face-centered cubic (fcc) phase of  $\text{Zn}_3[\text{Co}(\text{CN})_6]_2 \cdot n\text{H}_2\text{O}$  [space group:  $F43m$  (no. 216)] with lattice constant  $a = 10.41 \text{ \AA}$ , which is in good agreement with the standard values for bulk cubic  $\text{Zn}_3[\text{Co}(\text{CN})_6]_2 \cdot n\text{H}_2\text{O}$  (JCPDS no. 89-3739), and no other impurities are observed. Fig. 1b exhibits thermogravimetric analysis (TGA) curves of the  $\text{Zn}_3[\text{Co}(\text{CN})_6]_2 \cdot n\text{H}_2\text{O}$  precursor. It is found that  $\text{Zn}_3[\text{Co}(\text{CN})_6]_2 \cdot n\text{H}_2\text{O}$  underwent a sharp weight loss of 9.43% from room temperature to 130 °C, indicating the loss of water molecules from the porous framework structure. A second weight loss of 39.78% between 300 °C and 470 °C is possibly due to the release of  $\text{NO}_2$ ,  $\text{CO}_2$  and  $(\text{CN})_2$  gaseous molecules from the oxidation of the cyanide and residual PVP during the calcination process. Based on the TGA results, in

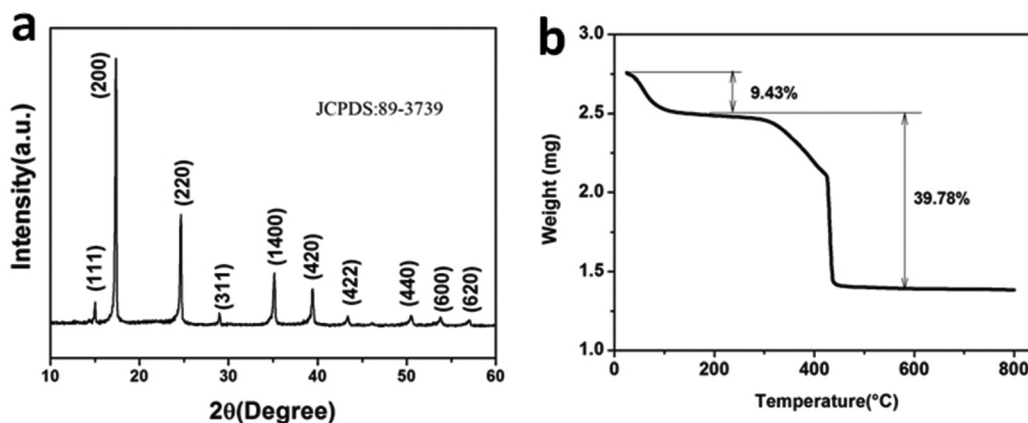


Fig. 1 (a) XRD pattern and (b) thermogravimetric analysis (TGA) of the as-prepared  $\text{Zn}_3[\text{Co}(\text{CN})_6]_2 \cdot n\text{H}_2\text{O}$  precursor.

order to ensure the calcination of the precursor completely, 500  $^{\circ}\text{C}$  was chosen as the calcination temperature for the decomposition of the  $\text{Zn}_3[\text{Co}(\text{CN})_6]_2 \cdot n\text{H}_2\text{O}$  precursor to  $\text{ZnO}/\text{Co}_3\text{O}_4$  nanocomposites. As expected, the  $\text{Zn}_3[\text{Co}(\text{CN})_6]_2 \cdot n\text{H}_2\text{O}$  precursor is thoroughly transformed into  $\text{ZnO}/\text{Co}_3\text{O}_4$  nanocomposites after annealing at 500  $^{\circ}\text{C}$  in air at a heating rate of 10  $^{\circ}\text{C min}^{-1}$ . Fig. 2 exhibits a typical XRD pattern of the as-obtained sample. The diffraction peaks marked '#' correspond to the standard patterns of the pure face-centered-cubic phase of spinel  $\text{Co}_3\text{O}_4$  with a lattice constant of  $a = 8.072 \text{ \AA}$  (JCPDS card no. 76-1802). And those marked '\*' can be indexed to the hexagonal  $\text{ZnO}$  (JCPDS card no. 36-1451). Because the (311) peak of  $\text{Co}_3\text{O}_4$  is very close to the (101) diffraction peak of  $\text{ZnO}$ , the two peaks were overlapped together and cannot be easily distinguished. No peak from the other undersigned phases was observed, indicating high purity of the as-obtained sample. Though the spinel phase  $\text{ZnCo}_2\text{O}_4$  is isostructural with  $\text{Co}_3\text{O}_4$  and it is difficult to clearly distinguish the

$\text{ZnCo}_2\text{O}_4$  and  $\text{Co}_3\text{O}_4$  phases from the XRD pattern, it is suggested that there is no spinel phase  $\text{ZnCo}_2\text{O}_4$  in the final sample according to our previous work.<sup>28</sup>

The size and morphology of  $\text{Zn}_3[\text{Co}(\text{CN})_6]_2 \cdot n\text{H}_2\text{O}$  precursors and porous  $\text{ZnO}/\text{Co}_3\text{O}_4$  nanocomposites were further investigated by field-emission scanning electron microscopy (FESEM). As shown in Fig. 3a and b, the  $\text{Zn}_3[\text{Co}(\text{CN})_6]_2 \cdot n\text{H}_2\text{O}$  products consist of many nanospheres with a size of approximately 220 nm and turn out to be large-scaled. This morphology is different from our previously reported nanocube-like Prussian blue analogue  $\text{Mn}_3[\text{Co}(\text{CN})_6]_2 \cdot n\text{H}_2\text{O}$  which was obtained in the

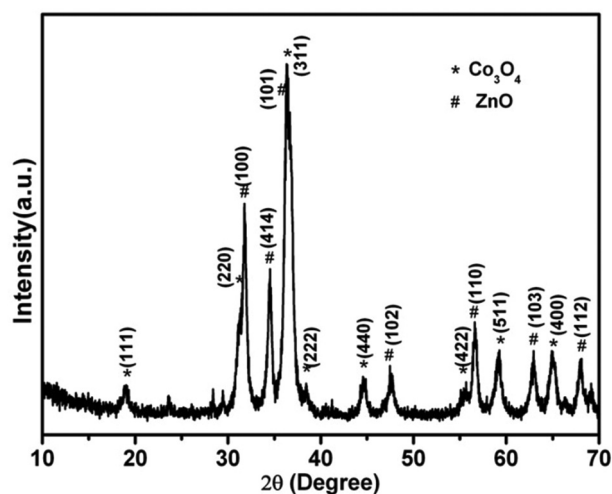


Fig. 2 XRD pattern of the  $\text{ZnO}/\text{Co}_3\text{O}_4$  nanocomposite.

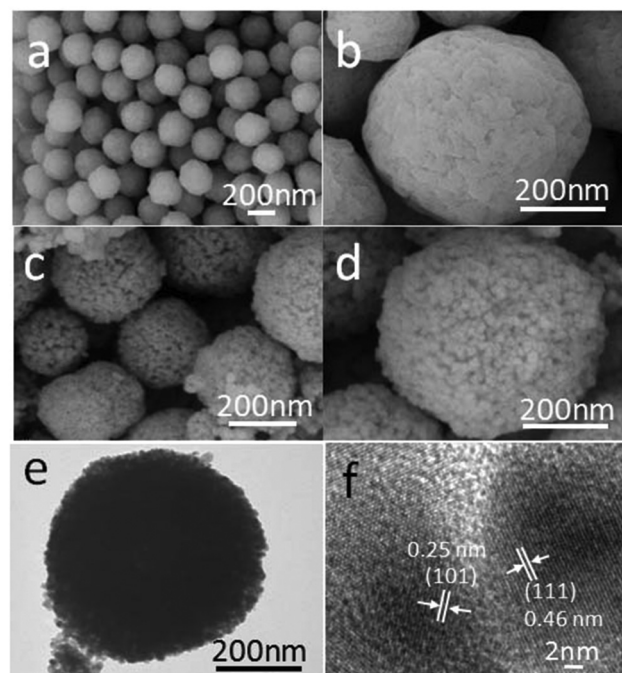


Fig. 3 SEM images of the as-prepared (a, b)  $\text{Zn}_3[\text{Co}(\text{CN})_6]_2 \cdot n\text{H}_2\text{O}$  and (c, d)  $\text{ZnO}/\text{Co}_3\text{O}_4$  nanocomposites at different magnifications. Typical TEM (e) and HRTEM (f) images of  $\text{ZnO}/\text{Co}_3\text{O}_4$  nanocomposites.

presence of PVP at room temperature.<sup>29</sup> The size of the  $\text{Zn}_3[\text{Co}(\text{CN})_6]_2 \cdot n\text{H}_2\text{O}$  precursor (approximately 200 nm) is also smaller than that of the previously reported  $\text{Zn}_3[\text{Co}(\text{CN})_6]_2 \cdot n\text{H}_2\text{O}$  microspheres (approximately 1  $\mu\text{m}$ ) obtained under ultrasonic conditions.<sup>30</sup> Fig. 3c and d show FESEM images of the as-prepared  $\text{ZnO}/\text{Co}_3\text{O}_4$  nanocomposites at different magnifications, demonstrating that they preserve well the uniform size and sphere-like morphology of the  $\text{Zn}_3[\text{Co}(\text{CN})_6]_2 \cdot n\text{H}_2\text{O}$  precursor particles. It is interesting to find that the surface of the sphere is very rough, indicating the gaseous molecule-derived (e.g.,  $\text{NO}_2$ ,  $\text{CO}_2$ ,  $(\text{CN})_2$ ) formation of abundant pores during the annealing process. Moreover, the simultaneous decomposition of organic linkers can also avoid the aggregation of the resulting nanometer-sized nanoparticles in the primary sphere-like  $\text{ZnO}/\text{Co}_3\text{O}_4$  nanocomposites, resulting in numerous mesopores in the structure of the sphere. Fig. 3e shows the typical transmission electron microscopy (TEM) image of the as-obtained porous  $\text{ZnO}/\text{Co}_3\text{O}_4$  nanocomposite. A large amount of well-distributed pores (the white points on the surface) can be clearly seen in the outline of the  $\text{ZnO}/\text{Co}_3\text{O}_4$  nanocomposite, indicating the product as an aggregation of nanocrystals. The heterojunction region between  $\text{ZnO}$  and  $\text{Co}_3\text{O}_4$  is also obviously shown in the high-resolution transmission electron microscopy (HRTEM) image (Fig. 3f). The measured neighbouring interlayer distance of 0.46 nm is consistent with the (111) plane of  $\text{Co}_3\text{O}_4$ , while that of 0.25 nm agrees with the (101) plane of  $\text{ZnO}$ .

To further investigate the specific surface areas and the porous nature of the as-obtained  $\text{ZnO}/\text{Co}_3\text{O}_4$  nanocomposites, Brunauer–Emmett–Teller (BET) gas-sorption measurements were performed. As shown in Fig. 4, the isotherm profile of the sample can be categorized as a type IV curve with a H3 hysteresis loop at the relative pressure of 0.8–1.0, thus implying the existence of a large number of mesopores in the  $\text{ZnO}/\text{Co}_3\text{O}_4$  nanocomposites. The Brunauer–Emmett–Teller

(BET) specific surface area of the  $\text{ZnO}/\text{Co}_3\text{O}_4$  nanocomposites was calculated to be  $46.9 \text{ m}^2 \text{ g}^{-1}$ , which is higher than that for  $\text{ZnFe}_2\text{O}_4/\alpha\text{-Fe}_2\text{O}_3$  nanocomposite based anode materials.<sup>31</sup> The pore-size distribution (the inset of Fig. 4) reveals a wide distribution centered at 17 nm, which are all in the range of mesopores. The narrow distribution was attributed to the porous nanocrystals, while the wide distribution was formed when the nanocrystals aggregated to form nanospheres. The mesoporous structure of the  $\text{ZnO}/\text{Co}_3\text{O}_4$  nanocomposites may facilitate the electrolyte to penetrate thoroughly into the pores and diffuse efficiently into active sites with less resistance, and also can relieve huge volume change during the charge/discharge process.

Fig. 5a exhibits the first three cyclic voltammetry (CV) curves of the  $\text{ZnO}/\text{Co}_3\text{O}_4$  electrode at a scan rate of  $0.1 \text{ mV s}^{-1}$  between 0.0 and 3.0 V. It is obviously observed that the first-cycle curve is substantially different from those of the subsequent cycles, particularly for the discharge branch. In the first cycle, the broad peak centered at 1.25 V can be ascribed to the reduction of  $\text{Zn}^{2+}$  and  $\text{Co}^{3+}$  or  $\text{Co}^{2+}$  to their metallic states, respectively, whereas the peak at 0.65 V can be assigned to irreversible decomposition of the electrolyte to form the solid-electrolyte interface (SEI) films.<sup>32–35</sup> The broad anode peak at approximately 1.30 V can be assigned to the oxidation of metallic Zn and Co to  $\text{Zn}^{2+}$  and  $\text{Co}^{3+}$  or  $\text{Co}^{2+}$ , respectively.<sup>34–36</sup> It is also found that the intensity of the cathodic peak drops significantly in the subsequent cycles relative to that in the first cycle, further indicating the occurrence of some irreversible reactions with the formation of the SEI film.<sup>37</sup> The peak intensity and integral area of the third cycle are almost the same as those of the second scan, indicating the good reversibility after the second cycle.

Recently, it was revealed that incorporation of  $\text{Ni}_3\text{ZnCo}_{0.7}$  into  $\text{ZnO}$  increased the reversible capacity of  $\text{ZnO}$  anodes, and  $\text{ZnO-NiO-C}$  films exhibited one of the highest capacities, best cyclabilities and fastest rate capabilities among the reported  $\text{ZnO}$ -based anodes.<sup>38</sup> In addition, lithium storage properties of porous  $\text{ZnCo}_2\text{O}_4$  nanostructures have been also studied.<sup>36</sup> Since the mesoporous  $\text{ZnO}/\text{Co}_3\text{O}_4$  nanocomposites possess bimodal pore-distribution and a relatively high surface area, they may be promising materials for LIBs. Fig. 5b shows the 1st, 2nd and 3rd discharge-charge curves of the electrodes made from the porous  $\text{ZnO}/\text{Co}_3\text{O}_4$  nanocomposites at a current density of  $100 \text{ mA g}^{-1}$  between 0.01 and 3.0 V. There is a flat discharge plateau at about 0.70 V in the first cycle, which then gradually decreases to 0.01 V. The flat plateau is substituted by the sloping curves after the first cycle, which can be attributed to the heterogeneous reaction mechanism between Li and the electrode material. From the profiles, it can be also observed that the electrode displays a very high initial discharge capacity of  $2049 \text{ mA h g}^{-1}$ , whereas a relatively low reversible capacity of  $1164 \text{ mA h g}^{-1}$  is achieved, resulting in an initial coulombic efficiency of 56.8%. The theoretical capacity is predicated by the conversion reaction mechanism and calculated by the number of transferred electronics in the reaction. Actually, the initial discharge capacity is always

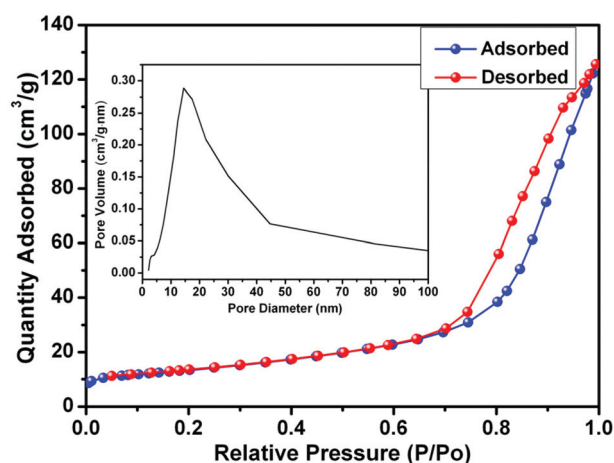


Fig. 4  $\text{N}_2$  adsorption/desorption isotherm (77 K) curves of  $\text{ZnO}/\text{Co}_3\text{O}_4$  nanocomposites and the inset of the pore volume vs. distribution of pore size.



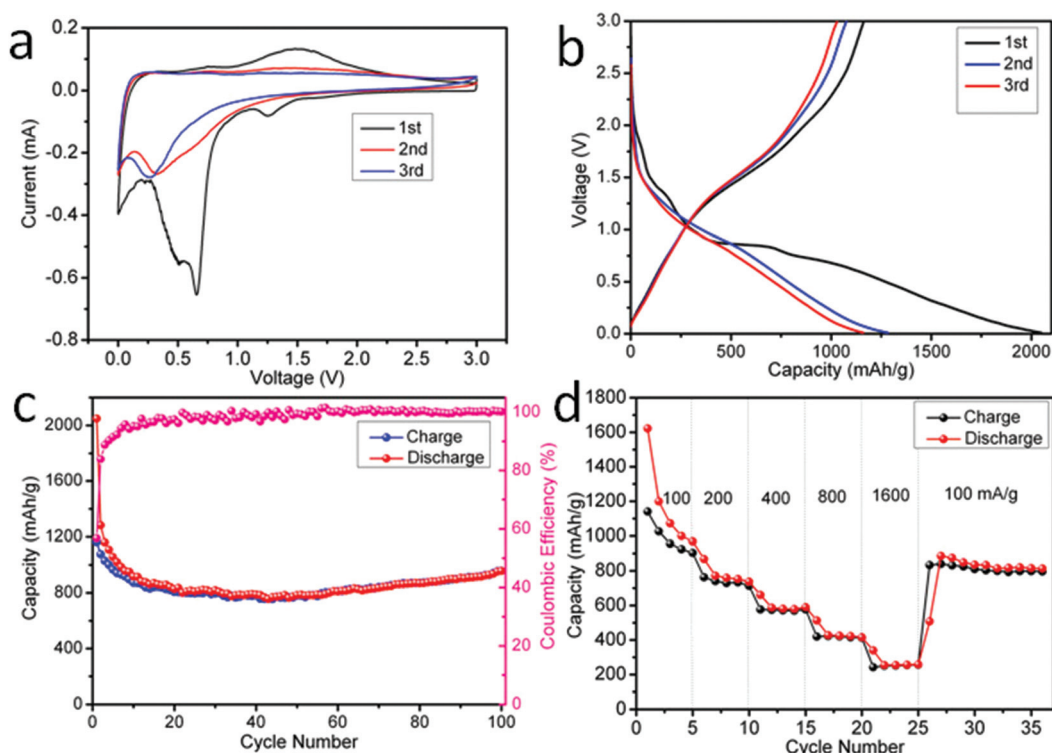


Fig. 5 Electrochemical properties of the ZnO/Co<sub>3</sub>O<sub>4</sub> nanocomposites for lithium storage. (a) The first three consecutive CV curves of the electrode prepared from ZnO/Co<sub>3</sub>O<sub>4</sub> nanocomposites. The voltage range was from 0.0 to 3.0 V at a scan rate of 0.1 mV s<sup>-1</sup>. (b) Discharge-charge curves at a current density of 100 mA g<sup>-1</sup>. (c) Cycling performance of the ZnO/Co<sub>3</sub>O<sub>4</sub> nanocomposites at a current density of 100 mA g<sup>-1</sup> in the voltage range of 0.01–3.0 V vs. Li/Li<sup>+</sup>. (d) Rate capability test for the ZnO/Co<sub>3</sub>O<sub>4</sub> nanocomposites at various current densities (100–1600 mA g<sup>-1</sup>).

higher than the theoretical capacity. The excess capacity can be attributed to the decomposition of the electrolyte to generate a solid electrolyte interface (SEI) layer and further lithium storage *via* interface charging at the metal/Li<sub>2</sub>O interface.<sup>39,40</sup> The relatively low initial coulombic efficiency can be attributed to the irreversible capacity loss, including decomposition of electrolytes, formation of SEI films, and some undecomposed Li<sub>2</sub>O phases, which are common for most anode materials.<sup>41,42</sup> The discharge capacities of the electrode in the 1<sup>st</sup>, 2<sup>nd</sup> and 3<sup>rd</sup> cycle are 2049, 1283 and 1161 mA h g<sup>-1</sup>, respectively.

Fig. 5c shows the cycling performance of the ZnO/Co<sub>3</sub>O<sub>4</sub> nanocomposites at a current density of 100 mA h g<sup>-1</sup>. Furthermore, from the 10<sup>th</sup> cycle onward, the coulombic efficiency of the electrode is above 95%, indicating the excellent capacity retention of the electrode materials. It is also interesting to find that the discharge capacity decreases slightly during the first several dozens of cycles and then increases gradually to 957 mA h g<sup>-1</sup> after 100 cycles, which can be attributed to increased electrochemical access to the active material as cycling proceeds and the reversible growth of a polymeric gel-like film resulting from kinetically activated electrode degradation.<sup>43,44</sup> Fig. 5d exhibits the rate performance of the electrode at different current densities between 100 and 1600 mA g<sup>-1</sup>. When the current density was gradually increased from 100 to 200, 400, 800 and 1600 mA g<sup>-1</sup>, the corresponding dis-

charge capacities were 968, 737, 589, 416 and 259 mA h g<sup>-1</sup>, respectively. When the current density was again reduced from 1600 to 100 mA g<sup>-1</sup>, a reversible capacity of 813 mA h g<sup>-1</sup> was achieved. As we know, ZnO possesses a theoretical capacity of 978 mA h g<sup>-1</sup>, but it has rarely been used as anode material in lithium-ion batteries because ZnO exhibited poor cyclability compared with other transition metal oxides.<sup>45,46</sup> Although in previous reports pure Co<sub>3</sub>O<sub>4</sub> materials exhibited better lithium storage properties than that of our product, compared with lithium storage properties of ZnO, porous ZnO/Co<sub>3</sub>O<sub>4</sub> nanocomposites exhibit enhanced electrochemical properties.<sup>47–49</sup> Moreover, zinc is more environmentally benign, and much cheaper compared to cobalt. The results demonstrate that the ZnO/Co<sub>3</sub>O<sub>4</sub> nanocomposites have great potential as a high-performance anode material for LIBs. The excellent electrochemical performance can be attributed to the unique structural feature of the self-assembled ZnO/Co<sub>3</sub>O<sub>4</sub> nanocomposite clusters. On the one hand, the porous structures can effectively improve the electrochemical kinetics, shorten the transport pathways of lithium ions and electrons, and reduce the diffusion length and resistance for the transport of lithium ions and electrolyte molecules. On the other hand, the volume change can be efficiently relieved by porous structures with self-assembled ZnO/Co<sub>3</sub>O<sub>4</sub> nanocomposite clusters, thus maintaining the mechanical integrity and chemical stability of the

electrode during the charge/discharge process. Finally, the synergetic effect of  $\text{Co}_3\text{O}_4$  and  $\text{ZnO}$  may also contribute to the excellent electrochemical performance.<sup>50</sup> In addition, the introduction of  $\text{ZnO}$  into  $\text{ZnO}/\text{Co}_3\text{O}_4$  nanocomposite clusters can reduce the weight of  $\text{Co}_3\text{O}_4$  as anode materials, which is costly and toxic, and the nanocomposite clusters simultaneously exhibit excellent electrochemical performance.

## 4. Conclusions

In summary, porous  $\text{ZnO}/\text{Co}_3\text{O}_4$  nanocomposites have been successfully synthesized through a simple strategy, which involves the room-temperature fabrication of the  $\text{Zn}_3[\text{Co}(\text{CN})_6]_2$  precursor and subsequent thermal decomposition of the precursor at 500 °C in air. When evaluated as anode materials for LIBs, the as-synthesized  $\text{ZnO}/\text{Co}_3\text{O}_4$  nanocomposites exhibit a high reversible capacity of 957 mA h g<sup>-1</sup> after 100 cycles at a current density of 100 mA g<sup>-1</sup>. The excellent cycling performance and high capacity can be attributed to their porous structures with self-assembled  $\text{ZnO}/\text{Co}_3\text{O}_4$  nanocomposite clusters. This work may also provide a general method to design and prepare porous composite metal oxides for extensive applications in high-performance LIBs, supercapacitors, and catalysis.

## Acknowledgements

This work was supported by the National Natural Science Foundation (NSFC, 21371009, U1232211) and Natural Science Foundation of Anhui Provincial Education Department (KJ2014A146).

## References

- 1 A. R. Armstrong, C. Lyness, P. M. Panchmatia, M. S. Islam and P. G. Bruce, *Nat. Mater.*, 2011, **10**, 223–229.
- 2 M. V. Reddy, G. V. S. B. Rao and V. R. Chowdari, *Chem. Rev.*, 2013, **113**, 5364–5457.
- 3 M. V. Reddy, G. Prithvi, K. P. Loh and B. V. R. Chowdari, *ACS Appl. Mater. Interfaces*, 2014, **6**, 680–690.
- 4 S. M. Xu, C. M. Hessel, H. Ren, R. B. Yu, Q. Jin, M. Yang, H. J. Zhao and D. Wang, *Energy Environ. Sci.*, 2014, **7**, 632–637.
- 5 D. W. Su, M. Ford and G. X. Wang, *Sci. Rep.*, 2012, **2**, 924.
- 6 Y. J. Zhang, Y. Yan, X. Y. Wang, G. Li, D. R. Deng, L. Jiang, C. Y. Shu and C. R. Wang, *Chem. – Eur. J.*, 2014, **20**, 6126–6130.
- 7 X. W. Li, S. L. Xiong, J. F. Li, X. Liang, J. Z. Wang, J. Bai and Y. T. Qian, *Chem. – Eur. J.*, 2013, **19**, 11310–11319.
- 8 F. C. Zheng, D. Q. Zhu and Q. W. Chen, *ACS Appl. Mater. Interfaces*, 2014, **6**, 9256–9264.
- 9 S. J. Yang, S. Nam, T. Kim, J. H. Im, H. Jung, J. H. Kang, S. G. Wi, B. Park and C. R. Park, *J. Am. Chem. Soc.*, 2013, **135**, 7394–7397.
- 10 L. W. Yin, Z. W. Zhang, Z. Q. Li, F. B. Hao, Q. Li, C. X. Wang, R. H. Fan and Y. X. Qi, *Adv. Funct. Mater.*, 2014, **24**, 4176–4185.
- 11 F. Zou, X. L. Hu, Z. Li, L. Qie, C. C. Hu, R. Zeng, Y. Jiang and Y. H. Huang, *Adv. Mater.*, 2014, **26**, 6622–6628.
- 12 J. Bai, X. G. Li, G. Z. Liu, Y. T. Qian and S. L. Xiong, *Adv. Funct. Mater.*, 2014, **24**, 3012–3020.
- 13 K. Su, C. Wang, H. G. Nie, Y. Guan, F. Liu and J. T. Chen, *J. Mater. Chem. A*, 2014, **2**, 10000–10006.
- 14 X. Z. Wang, S. Qiu, G. X. Lu, C. Z. He, J. R. Liu, L. Q. Luan and W. Liu, *CrystEngComm*, 2014, **16**, 1802–1809.
- 15 R. Z. Jin, Z. Bian, J. Z. Li, M. X. Ding and L. X. Gao, *Dalton Trans.*, 2013, **42**, 3936–3940.
- 16 X. D. Xu, R. G. Cao, S. Jeong and J. Cho, *Nano Lett.*, 2012, **12**, 4988–4991.
- 17 F. C. Zheng, D. Q. Zhu, X. H. Shi and Q. W. Chen, *J. Mater. Chem. A*, 2015, **3**, 2815–2824.
- 18 S. J. Yang and C. R. Park, *Adv. Mater.*, 2012, **24**, 4010–4013.
- 19 C. H. Kuo, Y. Tang, L. Y. Chou, B. T. Sneed, C. N. Brodsky, Z. P. Zhao and C. K. Tsung, *J. Am. Chem. Soc.*, 2012, **134**, 14345–14348.
- 20 L. Hu and Q. W. Chen, *Nanoscale*, 2014, **6**, 1236–1257.
- 21 S. J. Yang, S. Nam, T. Kim, J. H. Im, H. Jung, J. H. Kang, S. G. Wi, B. Park and C. R. Park, *J. Am. Chem. Soc.*, 2013, **135**, 7394–7397.
- 22 R. B. Wu, X. K. Qian, K. Zhou, J. Wei, J. Lou and P. M. Ajayan, *ACS Nano*, 2014, **8**, 6297–6303.
- 23 B. Liu, H. Shioyama, T. Akita and Q. Xu, *J. Am. Chem. Soc.*, 2008, **130**, 5390–5391.
- 24 F. C. Zheng, M. N. He, Y. Yang and Q. W. Chen, *Nanoscale*, 2015, **7**, 3410–3417.
- 25 L. Hu, N. Yan, Q. W. Chen, P. Zhang, H. Zhong, X. R. Zheng, Y. Li and X. Y. Hu, *Chem. – Eur. J.*, 2012, **18**, 8971–8977.
- 26 F. C. Zheng, Y. Yang and Q. W. Cheng, *Nat. Commun.*, 2014, **5**, 5261.
- 27 L. Zhang, H. B. Wu, S. Madhavi, H. H. Hng and X. W. Lou, *J. Am. Chem. Soc.*, 2012, **134**, 17388–17391.
- 28 L. Hu, P. Zhang, Y. K. Sun, S. X. Bao and Q. W. Chen, *ChemPhysChem*, 2013, **14**, 3953–3959.
- 29 L. Hu, P. Zhang, Q. W. Chen, N. Yan and J. Y. Mei, *Dalton Trans.*, 2011, **40**, 5557–5562.
- 30 D. J. Du, M. H. Cao, X. Y. He, Y. Y. Liu and C. W. Hu, *Langmuir*, 2009, **25**, 7057–7062.
- 31 D. Zhao, Y. Xiao, X. Wang, Q. Gao and M. H. Cao, *Nano Energy*, 2014, **7**, 124–133.
- 32 S. H. Choi and Y. C. Kang, *ChemSusChem*, 2013, **6**, 2111–2116.
- 33 M. P. Yu, A. J. Wang, Y. S. Wang, C. Li and G. Q. Shi, *Nanoscale*, 2014, **6**, 11419–11424.
- 34 M. A. Garakani, S. Abouali, B. Zhang, C. A. Takagi, Z. L. Xu, J. Q. Huang, J. Q. Huang and J. K. Kim, *ACS Appl. Mater. Interfaces*, 2014, **6**, 18971–18980.
- 35 Y. M. Sun, X. L. Hu, W. Lou, F. F. Xia and Y. H. Huang, *Adv. Funct. Mater.*, 2013, **23**, 2436–2444.

- 36 Y. Qiu, S. Yang, H. Deng, L. Jin and W. Li, *J. Mater. Chem.*, 2010, **20**, 4439–4444.
- 37 R. B. Wu, X. K. Qian, X. H. Rui, H. Liu, B. L. Yadian, K. Zhou, J. Wei, Q. Y. Yan, X. Q. Feng, Y. Long, L. Y. Wang and Y. Z. Haung, *Small*, 2014, **10**, 1932–1938.
- 38 Q. M. Pan, L. M. Qin, J. Liu and H. B. Wang, *Electrochim. Acta*, 2010, **55**, 5780–5785.
- 39 L. Hu, H. Zhong, X. R. Zheng, Y. M. Huang, P. Zhang and Q. W. Chen, *Sci. Rep.*, 2012, **2**, 986.
- 40 N. Yan, L. Hu, Y. Li, Y. Wang, H. Zhong, X. Y. Hu, X. K. Kong and Q. W. Chen, *J. Phys. Chem. C*, 2012, **116**, 7227–7235.
- 41 X. N. Li, Y. C. Zhu, X. Zhang, J. W. Liang and Y. T. Qian, *RSC Adv.*, 2013, **3**, 10001–10006.
- 42 C. X. Yang, Q. M. Gao, W. Q. Tian, Y. L. Tan, T. Zhang, K. Yang and L. H. Zhu, *J. Mater. Chem. A*, 2014, **2**, 19975–19982.
- 43 S. B. Wang, Y. B. Ren, G. R. Liu, Y. L. Xing and S. C. Zhang, *Nanoscale*, 2014, **6**, 3508–3512.
- 44 R. B. Wu, X. K. Qian, K. Zhou, J. Wei, J. Lou and P. M. Ajayan, *ACS Nano*, 2014, **8**, 6297–6303.
- 45 H. B. Wang, Q. M. Pan, Y. X. Cheng, J. W. Zhao and G. P. Yin, *Electrochim. Acta*, 2009, **54**, 2851–2855.
- 46 X. H. Huang, X. H. Xia, Y. F. Yuan and F. Zhou, *Electrochim. Acta*, 2011, **56**, 4960–4965.
- 47 L. Tian, H. L. Zou, J. X. Fu, X. F. Yang, Y. Wang, H. L. Guo, X. H. Fu, C. L. Liang, M. M. Wu, P. K. Shen and Q. M. Gao, *Adv. Funct. Mater.*, 2010, **20**, 617–623.
- 48 C. C. Li, X. M. Yin, Q. H. Li, L. B. Chen and T. H. Wang, *Chem. – Eur. J.*, 2011, **17**, 1596–1604.
- 49 J. Liu, H. Xia, L. Lu and D. F. Xue, *J. Mater. Chem.*, 2010, **20**, 1506–1510.
- 50 G. Huang, F. F. Zhang, L. L. Zhang, X. C. Du, J. W. Wang and L. M. Wang, *J. Mater. Chem. A*, 2014, **2**, 8048–8053.